Synthesis of Ag Loaded ZnO/BiOCl with High Photocatalytic Performance for the Removal of Antibiotic Pollutants

Zhihao Zhang [1], Amir Zada [2], Nan Cui [3], Naiwen Liu [3], Minghui Liu [3], Yuzhuo Yang [3], Delong Jiang [1,*], Jianhui Jiang [4,*] and Shuyuan Liu [5,*]

[1]   Jilin Institute of Chemical Technology, Jilin 132022, China; zhangzh202107@163.com
[2]   Department of Chemistry, Abdul Wali Khan University Mardan, Mardan 23200, Pakistan;
        amirzada@awkum.edu.pk
[3]   Institute of Catalysis for Energy and Environment, College of Chemistry and Chemical Engineering,
        Shenyang Normal University, Shenyang 110034, China; 15842743380@163.com (N.C.);
        naiwenliu2021@163.com (N.L.); lmh15241637597@163.com (M.L.); yangyuzhuo202107@163.com (Y.Y.)
[4]   College of Life Science, Tarim University, Alar 843300, China
[5]   Department of Pharmacology, Shenyang Medical College, Shenyang 110032, China
[*]   Correspondence: Isy_19870110@126.com (D.J.); xjjjh78@163.com (J.J.); liushuyuan@symc.edu.cn (S.L.)

Abstract: Ag@ZnO/BiOCl composites were successfully prepared by in situ precipitation and hydrothermal synthesis and used for the photocatalytic degradation of tetracycline hydrochloride antibiotics. An enhanced photodegradation efficiency was detected after loading Ag nanoparticles, which is attributed to the surface plasmon resonance effect. The optimized sample containing 4% Ag showed 80.4% degradation efficiency in 80 min, which is 2.1 and 1.9 times higher than those of ZnO and ZnO/BiOCl, respectively. The major degrading species involved in the photocatalytic process were detected to be super oxide anions and holes. Based on the obtained results, a possible charge transfer and degradation mechanism has been proposed. This study shows that Ag@ZnO/BiOCl catalyst has a good potential for photodegradation of organic pollutants in water.

Keywords: Ag@ZnO/BiOCl; photocatalyst; degradation; tetracycline hydrochloride; simulated solar light

1. Introduction

Tetracycline hydrochloride (TC–HCl) is a widely used antibiotic, and its production is second place in the world [1]. TC–HCl is discharged into the surrounding water environment through human and animal metabolism and pharmaceutical companies and enters the human body through the food chain [2]. The accumulation of TC–HCl and other antibiotics results in drug resistance pathogenic bacteria, and therefore has vast effects on human health and aquatic life [3]. In order to prevent their large scale accumulation in water, photocatalytic degradation with the help of photocatalysts such as TiO_2, ZnO, SnO_2, g-C_3N_4, etc., has been carried out in-depth [4–14]. However, most of the photocatalysts are only active under ultraviolet, which comprises a limited portion of the solar spectrum [15–24]. Therefore, it is necessary to find photocatalysts with good visible light absorption performance.

ZnO has the advantages of high electron mobility, non-toxicity, and high photosensitivity, with excellent activity for the photocatalytic degradation of organic pollutants in wastewater [25–27]. However, its wide band gap results in its poor light response in the visible range. In addition, the high recombination rate of photogenerated electrons and holes further retard its activity. Therefore, its combination with other semiconductors is highly appreciated to overcome these deficiencies. As a n-type semiconductor, its combination with p-type semiconductors such as BiOCl is an effective strategy to improve the photocatalytic activity by charge transfer and separation from BiOCl to ZnO [28].

Noble metals such as Au and Ag can be used as driving agents for photocatalytic performance when deposited on a photocatalyst surface to improve visible light absorption through their surface plasmon resonance effects [29–32]. The introduction of these metals not only enhances visible light absorption, but they also play a very important role in charge separation and surface catalysis due to their metallic nature. Particularly, the Ag nanoparticles formed by reduction of Ag^+ ions by oxygen vacancy are very attractive, as Ag is relatively chief compare to Au [33]. With the quenching of oxygen vacancy and plasma effect at the close interface between Ag and the semiconductor composites, Ag can be more efficient in the removal of organic pollutants in water system under visible light irradiation. Many experiments show that Ag nanoparticles can promote the photocatalytic reactions. For example, Christopher et al. prepared Ag and TiO_2 composite photocatalyst, which showed higher photo-responsive activity than pure TiO_2 in the photodegradation process of methylene blue [34]. The Ag modified ZnO nanorods were prepared by Ren et al., and the photocatalytic performance of Ag/ZnO for the degradation of methyl blue was greatly improved compared to pure ZnO nanorods [35]. Rupa et al. investigated the photocatalytic degradation of active yellow-17 by Ag–TiO_2 under light irradiation and found that TiO_2 deposited by Ag can promote the degradation process [36].

In this work, a series of ZnO/BiOCl composite photocatalysts were successfully prepared by hydrothermal synthesis and in situ coprecipitation and noble metal Ag was loaded on the surface of the ZnO/BiOCl to get Ag@ZnO/BiOCl composites. The as-prepared samples showed enhanced photocatalytic degradation activity for TC–HCl under the simulated solar light due to extended visible light absorption and improved charge separation. Based on the obtained results, a schematic showing charge transfer and separation has been proposed.

2. Experimental Section

2.1. Synthesis of ZnO Nanoparticles

For the preparation of ZnO nanoparticles, 1.317 g $Zn(CH_3COO)_2 \cdot 2H_2O$ (0.006 mol) were dissolved in 20 mL ultrapure water in a beaker. About 0.6 g NaOH (0.015 mol) were also dissolved in 20 mL water and added dropwise to $Zn(CH_3COO)_2 \cdot 2H_2O$ solution under constant stirring. The resultant solution was taken in 50 mL autoclave and heated at 140 °C for 12 h in an oven. The obtained precipitate was filtered, washed with deionized water and then dried at 80 °C in an oven. The dried sample was calcined at 450 °C for 60 min to get ZnO nanoparticles.

2.2. Synthesis of ZnO/BiOCl Nanocomposites

For the synthesis of ZnO/BiOCl composite, 1.616 g $Bi(NO_3)_3 \cdot 5H_2O$ (0.00333 mol) and 0.252 g KCl (0.00338) were dissolved in deionized water and mixed with 0.405 g ZnO nanoparticles. The suspension was stirred for 30 min and transferred to 50 autoclave. The autoclave was heated at 100 °C for 12 h. The obtained precipitate was filtered, washed with deionized water and then dried at 80 °C in an oven to get ZnO/BiOCl nanocomposite.

2.3. Synthesis of Ag Loaded ZnO/BiOCl Nanocomposites

For the preparation of Ag loaded ZnO/BiOCl nanocomposites, 0.2 g ZnO/BiOCl were dispersed in 60 mL ultrapure water under ultrasonication for 20 min. Different volumes of $AgNO_3$ solution (0.1 M, 1–7 mL) were added to the above solution dropwise and stirred in dark for 30 min. The well dispersed mixture was irradiated under a xenon light source for 1 h. The mixture centrifuged (7000 r/min, 10 min) after standing, and the precipitates were placed in a vacuum drying oven at 60 °C for 24 h to get gray black samples. According to the volume of the added silver nitrate, the theoretical Ag content is calculated to be 5, 10, 15, 20, 25, 30 and 35%. These samples were represented by X%-Ag@ZnO/BiOCl, where X% shows the percent amount of Ag in the nanocomposites.

2.4. Characterization

The Bruker D8 Advance X-ray diffractometer (XRD, Cu kα, λ = 1.54056 Å) was used to study the crystal phase of the samples. X-ray photoelectron spectroscopy (XPS) was measured on PHIQ1600 XPS (US) instrument. High resolution transmission electron microscopy (HRTEM) was carried out with Japanese JEOL-JEM-2100F electron microscope. The UV-Vis absorption spectra were collected on the Shimadzu UV3100 (Kyoto, Japan) spectrophotometer using $BaSO_4$ as reference. The photoluminescence (PL) spectra of ZnO and nanocomposite samples were studied on a Varian-Cary solar eclipse spectrometer with an excitation wavelength of 325 nm.

2.5. Photocatalytic Activity Measurements

The photocatalytic performance of the 4%-Ag@ZnO/BiOCl composites was tested by photocatalytic degradation of TC–HCl experiments using simulated solar light. As such, 32 mg Ag@ZnO/BiOCl catalysts were dispersed with 50 mL TC–HCl (20 mg/L) solution. The mixture was stirred in dark for 30 min to achieve adsorption of some amount of pollutant. About 5 mL solution was taken from it with the help of a disposable syringe, and the rest of the solution was irradiated under simulated solar light for 2 h, keeping the temperature constant at 25 °C. About 5 mL solution was drawn after each 20 min interval and the contents were centrifuged to remove the suspended particles. The sample was checked with UV-Vis spectrophotometer at 357 nm to measure the degradation rate and efficiency of Ag@ZnO/BiOCl. Furthermore, the effects of catalyst dosage, pH value and impurity ions on degradation were investigated.

3. Results and Discussion

3.1. XRD Analysis

The XRD patterns of ZnO, BiOCl and Ag@ZnO/BiOCl catalysts with different loading ratios are shown in Figure 1. The ZnO/BiOCl composites containing different Ag ratios have the same diffraction peaks, with the strong diffraction peak angles at 31.78, 34.42, 36.26, 47.54, 56.58, 62.84 and 67.94° corresponding, respectively, to the crystal faces (100), (002), (101), (102), (110), (103) and (112) of ZnO (PDF card 36-1451). The diffraction peaks at 12.05, 25.87, 32.56, 33.47 40.84, 46.78, 49.82, 54.12 and 58.74° correspond, respectively, to (001), (101), (110), (102), (112), (200), (113), (211) and (212) facets of BiOCl according to the standard PDF card (06-0249). The intensity of the diffraction peaks of the BiOCl at (101) and ZnO at (101) faces are obvious, which indicate that the Ag@ZnO/BiOCl composite is successfully prepared. With the increase of the loading amount, the (101) diffraction peak of ZnO decreases gradually, which is due the XRD diffraction intensity of BiOCl is relatively high. From the XRD data, there is no other impurity diffraction peak, indicating that the purity of the sample is high.
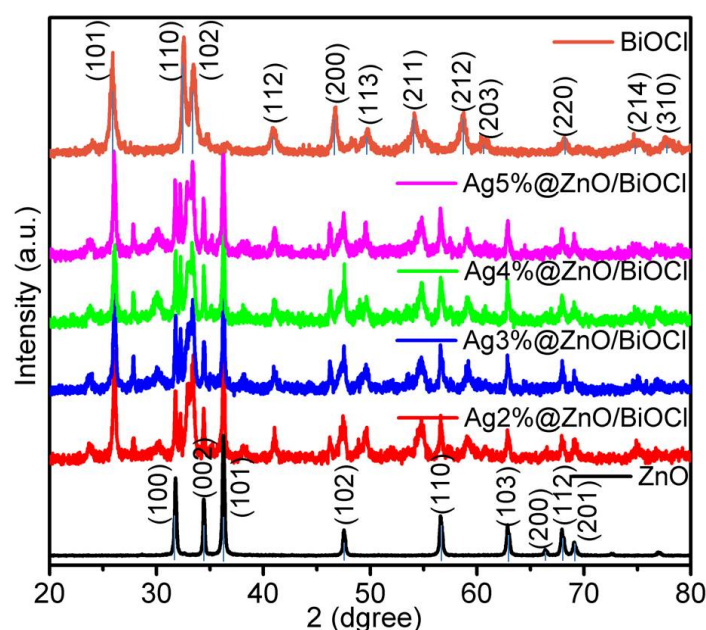
Figure 1. XRD patterns of ZnO and X%-Ag@ZnO/BiOCl samples.

3.2. Morphology Analysis

The morphology of the synthesized composites was studied by TEM measurements. It can be seen from Figure 2 that the two materials grow in two-dimensional layered structure, showing good structural lattice edge and excellent crystallinity of the prepared materials. ZnO is rod-shaped with a lattice spacing of 0.247 nm, corresponding to the (101) crystal surface of ZnO. BiOCl also shows a trend of longitudinal growth with a rod-shaped structure having lattice spacing of 0.275 nm with the (110) crystal facet. This indicates the successful construction of heterojunction between ZnO and BiOCl, which is very important for electrons transfer and conduction. Ag metal is present in the form of particles of 20 nm size. After Ag deposition, the smooth surface becomes rough, which is more conducive and provide large number of active sites. Additionally, according to SEM and corresponding elemental mapping images conducted for 4%-Ag@ZnO/BiOCl catalyst (Figure 3), it is confirmed the presence of Zn, O, Bi, Cl and Ag elements in the composite, wherein these elements are distributed evenly.
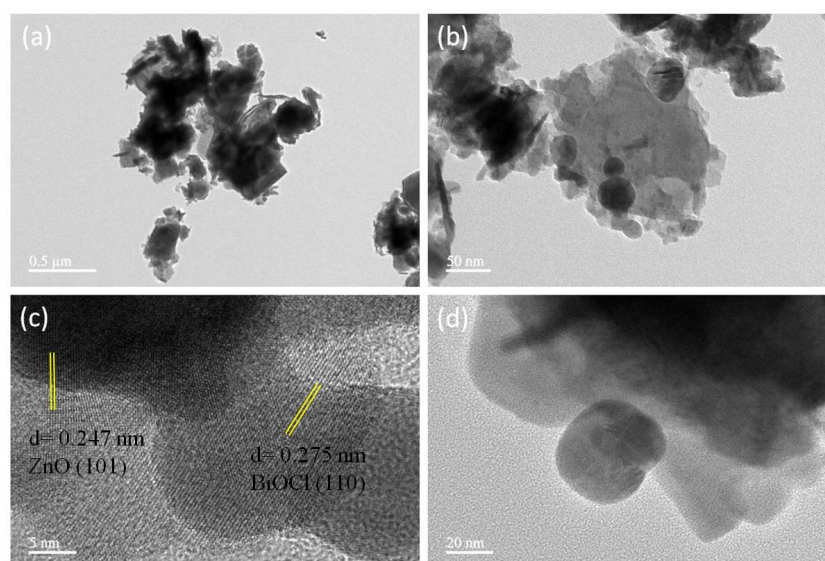

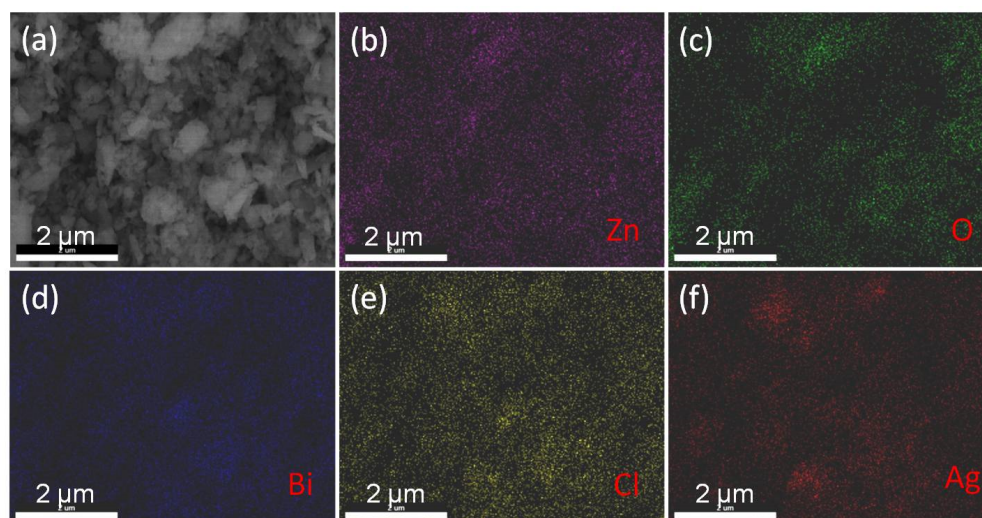**Figure 2.** (**a–d**)TEM images of 4%-Ag@ZnO/BiOCl catalyst.

Figure 3. SEM image and the corresponding elemental mapping images of 4%-Ag@ZnO/BiOCl catalyst (**a**–**f**).

3.3. XPS Analysis

Figure 4 shows the XPS energy spectra of 4%-Ag@ZnO/BiOCl. Obviously, there are Zn, O, Ag, Bi, Cl and C elements in the energy spectra showing the presence of these elements in 4%-Ag@ZnO/BiOCl, while the C peak mainly comes from the XPS instrument itself (Figure 4a). This indicates high purity of Ag loaded ZnO/BiOCl and successful construction of heterojunction between ZnO and BiOCl, which is consistent with the TEM results. The XPS binding energies of Zn2p in Figure 4b are located at 1044.8 and 1021.5 eV and correspond to the binding energy of $Zn2p_{1/2}$ and $Zn2p_{3/2}$ orbitals, respectively [37]. The biding energy peaks of Bi 4f in Figure 4c are deconvoluted into 164.2 and 159.1 eV which, respectively, correspond to $Bi4f_{5/2}$ and $Bi4f_{7/2}$. These energy peaks shows +3 valence state of Bi in ZnO/BiOCl composite [38]. The XPS spectrum of Cl 2p given in Figure 4d is composed of two strong peaks with binding energy at 199.8 and 198.3 eV and, respectively, corresponded to $Cl2p_{1/2}$ and $Cl2p_{3/2}$ orbitals of Cl^-. In addition, two asymmetric peaks in Figure 4e are the characteristic peaks of O1s, indicating that there are two different binding states of oxygen in the catalyst. The first peak is located at 531.5 eV, corresponding to Zn-O bond [37], while the 530.1 eV binding energy in the second peak corresponds to Bi-O bond in BiOCl layered structure. The high resolution Ag 3d spectrogram shows $Ag\ 3d_{5/2}$ and $Ag\ 3d_{3/2}$ orbitals, which correspond to Ag^+ and Ag^0, respectively (Figure 4f), indicate that Ag^+ has been successfully reduced to Ag^0.

3.4. UV-Vis DRS Analysis

In order to evaluate the light absorption properties of the samples, UV-Vis diffuse reflectance spectra were measured. Figure 5 shows that the material has obvious absorption in the near ultraviolet range. For ZnO, there is a typical absorption in the range of 200–400 nm, while the maximum absorption peak intensity of ZnO/BiOCl is lower than ZnO. However, the visible light absorption intensity of ZnO/BiOCl is slightly higher than ZnO. The light absorption edges of Ag@ZnO/BiOCl samples are almost the same in the ultraviolet region, but different in the visible region of 400–800 nm. Compare with pure ZnO, the Ag@ZnO/BiOCl composites show strong light absorption performance in the long wavelength range, and the absorption spectrum of the composite shows absorption in the range of 200–800 nm, which enhances the intrinsic absorption characteristics of ZnO [39]. This shows that Ag loading significantly increases the light absorption capacity of ZnO/BiOCl for extended photocatalysis.
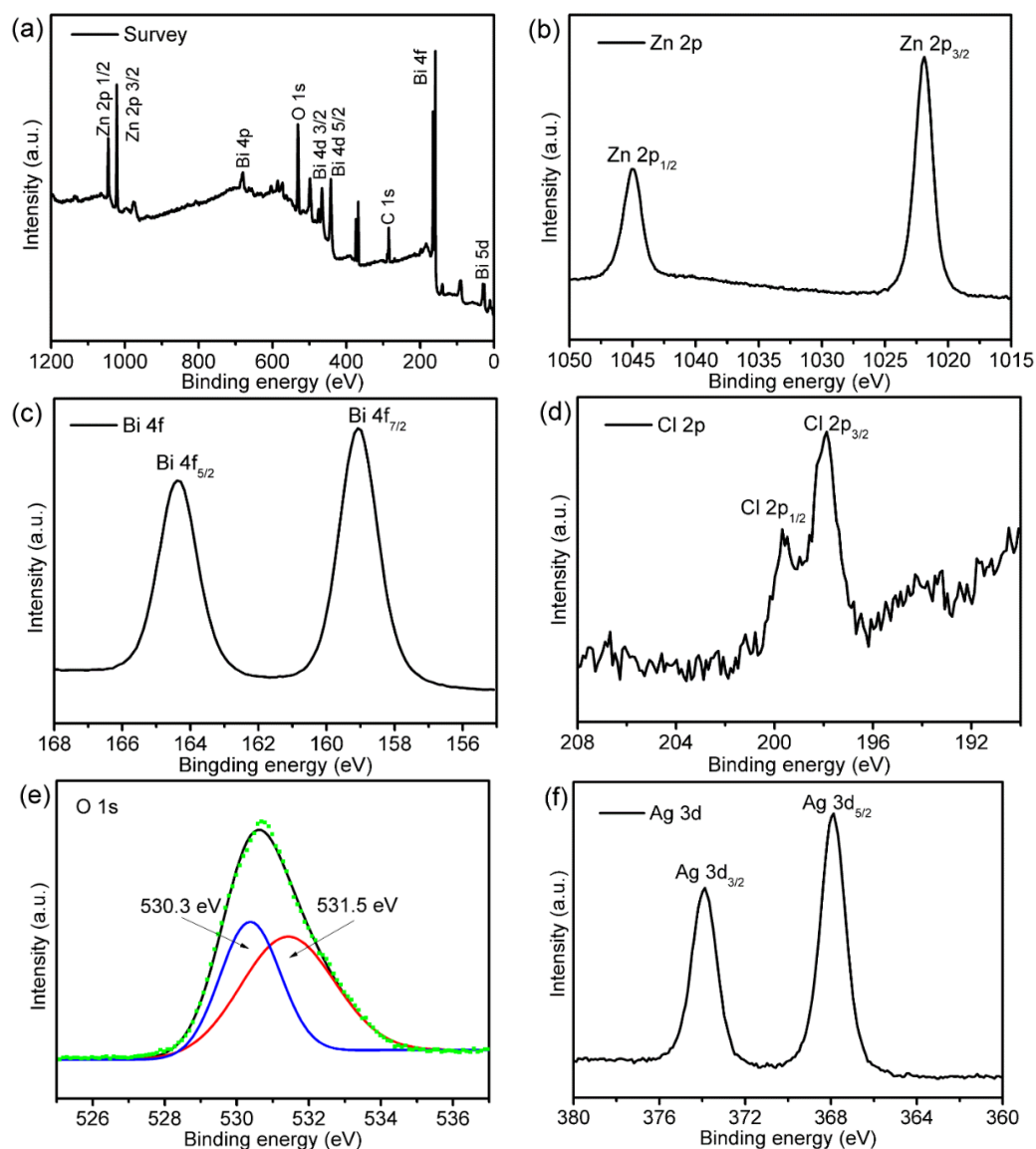
Figure 4. XPS survey spectra of 4%-Ag@ZnO/BiOCl (**a**), Zn 2p (**b**), Bi 4f (**c**), Cl 2p (**d**), O 1s (**e**) and Ag 3d (**f**).
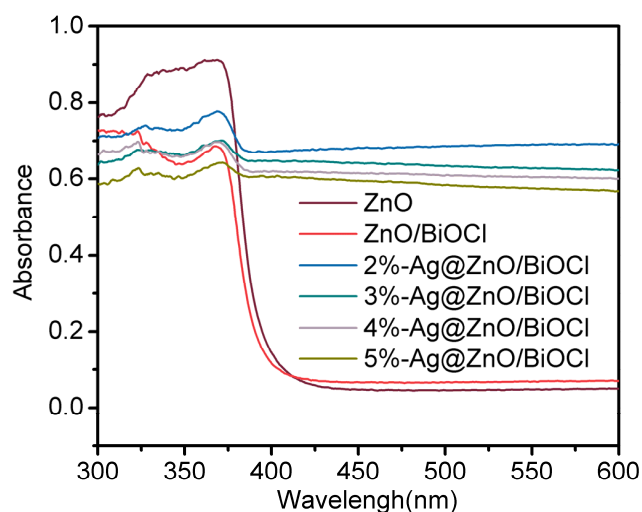

Figure 5. DRS spectrum of pure ZnO and Ag@ZnO/BiOCl samples.

3.5. PL Analysis

The photoluminescence (PL) spectra provide information about the separation and transportation of photogenerated carriers. Therefore, PL spectra of the samples were measured at 357 nm excitation wavelength, and the results are shown in Figure 6. There is a strong fluorescence emission peak at 450 nm for all the three samples. The photoelectric properties of ZnO have obvious changes after heterojunction formation with BiOCl and loading Ag nanoparticles. The order of the spectral intensity from strong to weak is: ZnO > ZnO/BiOCl > 4%-Ag@ZnO/BiOCl, which shows that 4%-Ag@ZnO/BiOCl has the largest fluorescence quenching, the most inhibition of electron–hole pair recombination, and the highest efficiency of photogenerated carrier separation [40]. The electron capturing property of Ag nanoparticles results in the effective transport and migration of excited electrons resulting in the increased separation of photogenerated electron–hole pairs, which lays a certain foundation for the active radicals needed in the subsequent reactions. Under simulated solar light irradiation, the excitation of Ag inducts excited electrons to the conduction band of ZnO, which provides other ways for photogenerated charge transfer to suppress the fluorescence quenching of ZnO and the recombination of photogenerated electron–hole pairs.
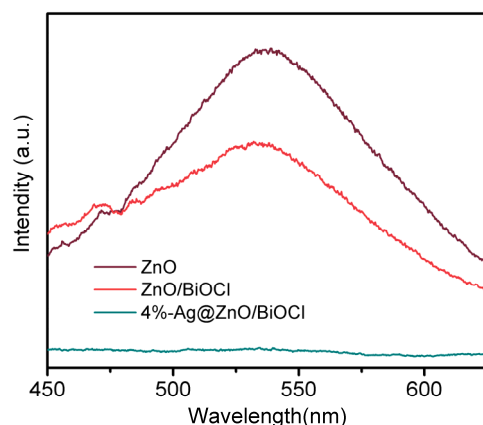

Figure 6. PL spectrum of pure ZnO, ZnO/BiOCl and 4%-Ag@ZnO/BiOCl samples.

4. Photocatalytic Activity

4.1. Photocatalytic Activity of Ag@ZnO/BiOCl

Figure 7 shows the time-dependent concentration of TC–HCl degraded by Ag@ZnO/BiOCl nanocomposites with different amounts of Ag nanoparticles under simulated solar light. The pH value of the reaction solution is 8. In the reaction process, the temperature is 25 °C and dark reaction time is 30 min, taking samples every 20 min. With the increase of Ag loading, the catalytic activity of Ag@ZnO/BiOCl increases first and then decreases. The photocatalytic activity of ZnO is low, and the degradation rate is 38.5% in 80 min. The degradation efficiency of ZnO/BiOCl is slightly higher, reaching 42.7%. Interestingly, the activities of all Ag loaded samples are higher than ZnO/BiOCl, and the degradation activity of 4%Ag nanocomposite is the highest with 80.4% removal efficiency. The kinetic curves of the photodegradation of TC–HCl agree with the quasi-first order kinetics. The k value of 4%-Ag@ZnO/BiOCl is the largest, which is three times more than that of ZnO. These improved photoactivities of Ag loaded samples are attributed to more visible light absorption and enhanced charge separation due to surface plasmon resonance and electron trapping ability of Ag and improved surface catalysis due to metallic Ag. However, further increase in the amount of Ag decreases the degradation activity, which may be attributed to the aggregation of Ag nanoparticles at high concentrations. Thus, the introduction of noble metals is a feasible strategy to improve the photocatalytic efficiency of large band gap semiconductors.
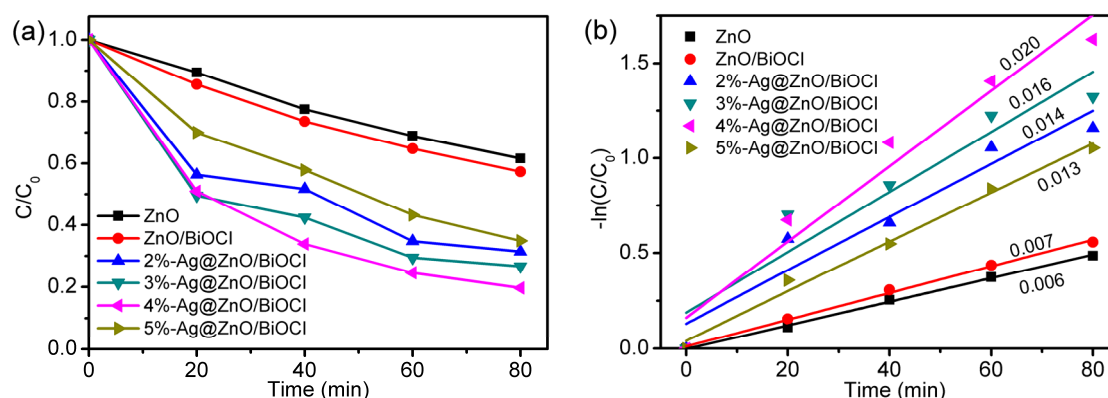
Figure 7. Photocatalytic degradation (**a**) and rate curve (**b**) of TC–HCl by ZnO, ZnO/BiOCl and Ag@ZnO/BiOCl.

4.2. Effect of Catalyst Amount

The amount of photocatalyst has a great influence on the overall photocatalytic efficiency. Figure 8 shows the degradation curve of TC–HCl (20 mg/L) in the presence of different dosages of the optimized photocatalyst under simulated solar light. When the amount of the photocatalyst is increased from 20 to 32 mg per 50 mL of the pollutant solution, the degradation efficiency is increased from 50 to 82.6%. This increase in the photoactivity is attributed to the adsorption of more pollutant particles available for the degradation under high amount of photocatalyst. However, when the amount of the photocatalyst is further increased to 40 mg, the photocatalytic efficiency is decreased to 70.1%. This decrease in photocatalytic activity is attributed to the turbidity of the solution resulting in poor light transmittance at too much high concentration of the photocatalyst. Another reason is the aggregation of the particles of the photocatalysts at high concentration, which reduce the specific surface and results in lower activity. Thus, the optimum amount of photocatalyst in this experiment is 32 mg per 50 mL of pollutant.
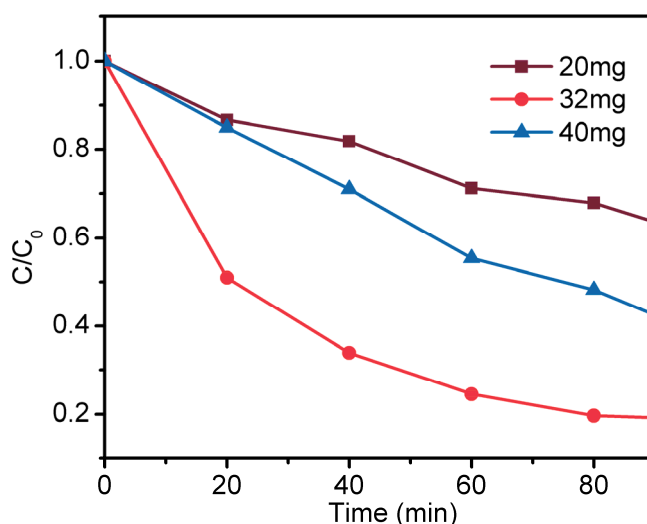

Figure 8. Photocatalytic degradation of TC–HCl by 4%-Ag@ZnO/BiOCl dosage.

4.3. Effect of Impurity Ions

The photodegradation efficiency of TC–HCl pollutants is examined with adding different impurity anions such as Cl^-, SO_4^{2-}, CO_3^{2-}, PO_4^{3-} and NO_3^- (Figure 9). The photoactivities are a little decreased after adding all these anions than that the photocatalytic activity of 4%-Ag@ZnO/BiOCl without adding of anions. The different photocatalytic performance is due to the different tendencies of the anions to be oxidized by the photo-

generated reactive oxygen species. These anions consume some of reactive oxygen species to prevent the decomposition of TC–HCl pollutants.
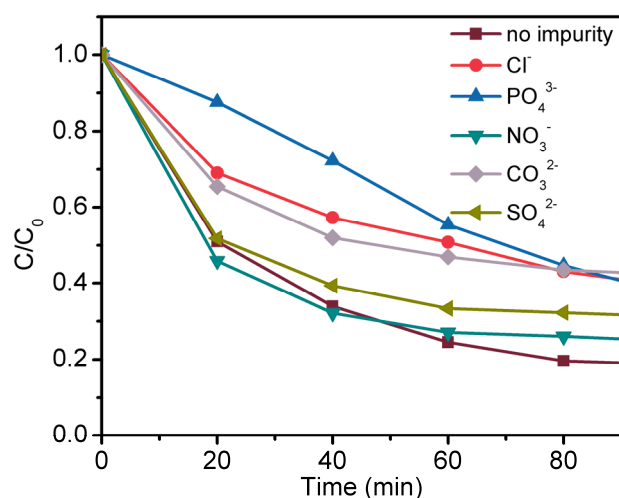
Figure 9. Photodegradation of TC–HCl by 4%-Ag@ZnO/BiOCl under different impurity ions.

4.4. Active Species

During photocatalysis, different free radicals are generated when the excited electrons and holes are captured by water and other substances in aqueous solution. These free radicals are highly reactive and take part in the oxidation of the pollutants. It is very important to find out the major oxidizing radical involved in the degradation of TC–HCl. For this purpose, the active oxygen species are examined by free radical capturing experiments, as shown in Figure 10. Ascorbic acid, triethanolamine, and iso-propyl alcohol are used as sacrificial agents for $^{\bullet}O_2^{-}$, h^+ and $^{\bullet}OH$, respectively. When ascorbic acid or triethanolamine is added to the reaction solution, the photocatalytic activity of 4%-Ag@ZnO/BiOCl is dramatically decreased. This indicates that $^{\bullet}O_2^{-}$ and h^+ play important roles in the photodegradation of TC–HCl. When iso-propyl alcohol is added into the reaction solution, the effect on the photocatalytic degradation is not obvious, which indicates that $^{\bullet}OH$ is not the main species affecting the photocatalytic performance. Thus, the main active oxygen species affecting the photocatalytic activity are h^+ and $^{\bullet}O_2^{-}$.
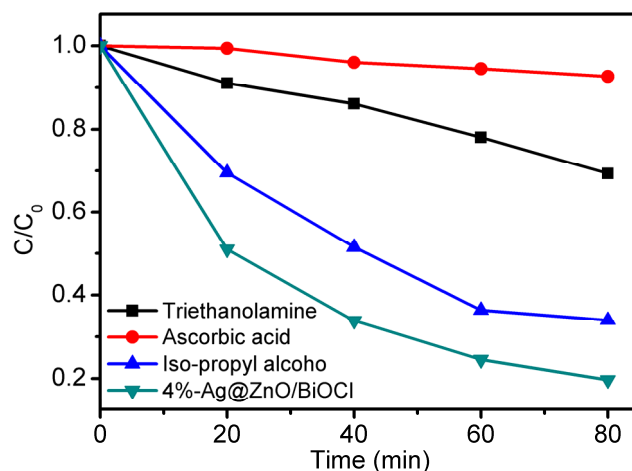
Figure 10. Photodegradation of TC–HCl by 4%-Ag@ZnO/BiOCl under different trapping agents.

4.5. Photocatalytic Mechanism

A schematic has been proposed indicating the charge separation and transfer in 4%-Ag@ZnO/BiOCl and possible photocatalytic degradation mechanism of TC–HCl as

shown in Figure 11. Before heterojunction construction, the Fermi levels of n-type ZnO are closed to its conduction band while the Fermi level of p-type BiOCl are closed to its valence band. There is a great difference between the Fermi level potentials of the two materials. When the two materials are compounded to form heterojunction, the Fermi levels are stabilized at the same potential, and the electrons and holes are transferred to the surface of the material at the same time. Under simulated solar light irradiation, both BiOCl and ZnO produce photogenerated electron–hole pairs, the photoexcited electrons in the conduction band (CB) of BiOCl are transferred to the conduction band of ZnO through the heterojunctional interface as the CB of BiOCl lies above the CB of ZnO. Since the valance band (VB) of BiOCl lies above the VB of ZnO, the holes remain the in the VB of BiOCl, which improves the separation efficiency of photogenerated electron–hole pairs to improve the photocatalytic degradation efficiency. These electrons in the CB of ZnO combine with adsorbed O_2 molecules to form $^\bullet O_2{}^-$, which are the major degrading species in the degradation of TC–HCl by Ag@ZnO/BiOCl. The introduction of Ag induces surface plasmon resonance excited electrons to the CB of ZnO to further enhance the formation of $^\bullet O_2{}^-$ and hence improves photocatalytic degradation. The excited holes in the VB of the BiOCl on the surface of Ag nanoparticles participate in the oxidation reaction. Thus, the introduction of Ag nanoparticles not only improve charge separation and light absorption of Ag@ZnO/BiOCl nanocomposite, but also plays very important role in the degradation of TC–HCl through surface catalysis.
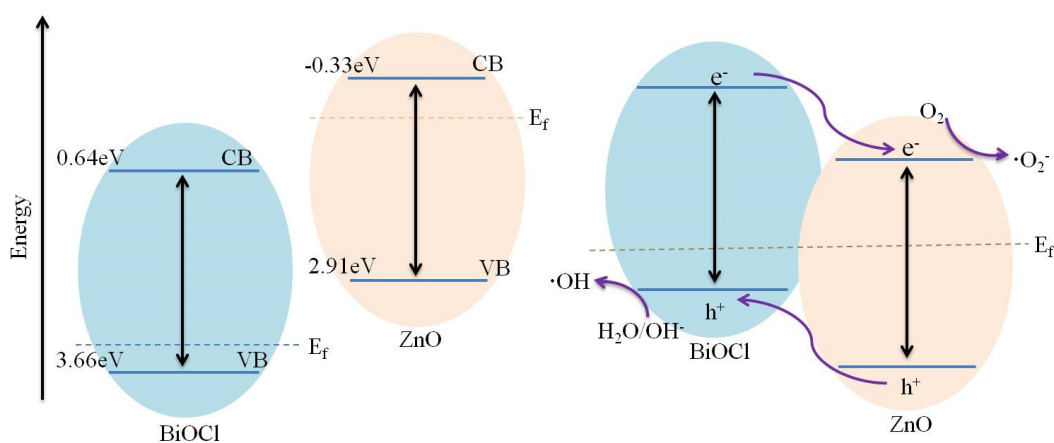

Figure 11. Ag@ZnO/BiOCl photocatalytic mechanism diagram.

5. Conclusions

In this work, ZnO/BiOCl nanocomposites modified by Ag nanoparticles were prepared by in situ precipitation and hydrothermal synthesis. The samples were adequately characterized and applied for the photocatalytic degradation of tetracycline hydrochloride. After loading Ag nanoparticles, the visible light response range of Ag@ZnO/BiOCl composite was extended, and its photocatalytic activity was enhanced. The improvement of the photocatalytic activity of Ag@ZnO/BiOCl is due to the surface plasmon resonance effect and enhanced charge separation of Ag nanoparticles. The optimized sample, i.e., 4%-Ag@ZnO/BiOCl showed, respectively, 2.3 and 1.6 times enhanced degradation efficiency than ZnO and ZnO/BiOCl. The Ag@ZnO/BiOCl catalyst has a good potential for the degradation of organic pollutants in water, considering the simplicity of the preparation process and utilization of visible light.

Author Contributions: Data curation, N.L., M.L. and D.J.; Formal analysis, N.C., Y.Y. and J.J.; Investigation, Z.Z.; Methodology, A.Z. and J.J.; Writing—original draft, N.L. and M.L.; Writing—review & editing, S.L. All authors have read and agreed to the published version of the manuscript.

Data Availability Statement: Not applicable.

Conflicts of Interest: The authors declare no conflict of interest.

References

1. Malesic-Eleftheriadou, N.; Evgenidou, E.N.; Kyzas, G.Z.; Bikiaris, D.N.; Lambropoulou, D.A. Removal of antibiotics in aqueous media by using new synthesized bio-based poly(ethylene terephthalate)-TiO$_2$ photocatalysts. *Chemosphere* **2019**, *234*, 746–755. [CrossRef] [PubMed]
2. Fan, X.; Gao, J.; Li, W.; Huang, J.; Yu, G. Determination of 27 pharmaceuticals and personal care products (PPCPs) in water: The benefit of isotope dilution. *Front. Environ. Sci. Eng.* **2019**, *14*, 8. [CrossRef]
3. Dehghan, A.; Zarei, A.; Jaafari, J.; Shams, M.; Mousavi Khaneghah, A. Tetracycline removal from aqueous solutions using zeolitic imidazolate frameworks with different morphologies: A mathematical modeling. *Chemosphere* **2019**, *217*, 250–260. [CrossRef] [PubMed]
4. Li, W.; Zhuang, C.; Li, Y.; Gao, C.; Jiang, W.; Sun, Z.; Qi, K. Anchoring ultra-small TiO$_2$ quantum dots onto ultra-thin and large-sized Mxene nanosheets for highly efficient photocatalytic water splitting. *Ceram. Int.* **2021**, *47*, 21769–21776. [CrossRef]
5. Yang, X.; Tian, J.; Guo, Y.; Teng, M.; Liu, H.; Li, T.; Lv, P.; Wang, X. ZnO Nano-Rod Arrays Synthesized with Exposed {0001} Facets and the Investigation of Photocatalytic Activity. *Crystals* **2021**, *11*, 522. [CrossRef]
6. Qi, K.; Zada, A.; Yang, Y.; Chen, Q.; Khataee, A. Design of 2D–2D NiO/g-C$_3$N$_4$ heterojunction photocatalysts for degradation of an emerging pollutant. *Res. Chem. Intermed.* **2020**, *46*, 5281–5295. [CrossRef]
7. Zhang, H.; Li, Y.; Li, W.; Zhuang, C.; Gao, C.; Jiang, W.; Sun, W.; Qi, K.; Sun, Z.; Han, X. Designing large-sized cocatalysts for fast charge separation towards highly efficient visible-light-driven hydrogen evolution. *Int. J. Hydrogen Energy* **2021**, *46*, 28545–28553. [CrossRef]
8. Zada, A.; Khan, M.; Qureshi, M.N.; Liu, S.-y.; Wang, R. Accelerating Photocatalytic Hydrogen Production and Pollutant Degradation by Functionalizing g-C$_3$N$_4$ With SnO$_2$. *Front. Chem.* **2020**, *7*, 941. [CrossRef]
9. Qi, K.; Cheng, B.; Yu, J.; Ho, W. A review on TiO$_2$-based Z-scheme photocatalysts. *Chin. J. Catal.* **2017**, *38*, 1936–1955. [CrossRef]
10. Liu, S.-y.; Ru, J.; Liu, F. NiP/CuO composites: Electroless plating synthesis, antibiotic photodegradation and antibacterial properties. *Chemosphere* **2021**, *267*, 129220. [CrossRef]
11. Al Suliman, N.; Awada, C.; Alshoaibi, A.; Shaalan, N.M. Simple Preparation of Ceramic-Like Materials Based on 1D-Agx(x=0, 5, 10, 20, 40 mM)/TiO2 Nanostructures and Their Photocatalysis Performance. *Crystals* **2020**, *10*, 1024. [CrossRef]
12. Li, C.; Wu, X.; Shan, J.; Liu, J.; Huang, X. Preparation, Characterization of Graphitic Carbon Nitride Photo-Catalytic Nanocomposites and Their Application in Wastewater Remediation: A Review. *Crystals* **2021**, *11*, 723. [CrossRef]
13. Zhu, Z.; Han, S.; Cao, Y.; Jiang, J. Synthesis of a Novel Photocatalyst MVO$_4$/g-C$_3$N$_4$ (M = La, Gd) with Better Photocatalytic Activity for Tetracycline Hydrochloride Degradation under Visible-Light Irradiation. *Crystals* **2021**, *11*, 756. [CrossRef]
14. Jin, Y.; Xing, Z.; Li, Y.; Han, J.; Lorenz, H.; Chen, J. Synthetic BiOBr/Bi2S$_3$/CdS Crystalline Material and Its Degradation of Dye under Visible Light. *Crystals* **2021**, *11*, 899. [CrossRef]
15. Qi, K.; Lv, W.; Khan, I.; Liu, S.-y. Photocatalytic H$_2$ generation via CoP quantum-dot-modified g-C$_3$N$_4$ synthesized by electroless plating. *Chin. J. Catal.* **2020**, *41*, 114–121. [CrossRef]
16. Ruqaishy, M.A.; Marzouqi, F.A.; Qi, K.; Liu, S.-Y.; Karthikeyan, S.; Kim, Y.; Al-Kindy, S.M.Z.; Kuvarega, A.T.; Selvaraj, R. Template-free preparation of TiO$_2$ microspheres for the photocatalytic degradation of organic dyes. *Korean J. Chem. Eng.* **2018**, *35*, 2283–2289. [CrossRef]
17. He, W.; Wu, H.; Wamer, W.G.; Kim, H.-K.; Zheng, J.; Jia, H.; Zheng, Z.; Yin, J.-J. Unraveling the Enhanced Photocatalytic Activity and Phototoxicity of ZnO/Metal Hybrid Nanostructures from Generation of Reactive Oxygen Species and Charge Carriers. *ACS Appl. Mater. Interfaces* **2014**, *6*, 15527–15535. [CrossRef]
18. Praus, P.; Svoboda, L.; Dvorský, R.; Reli, M. Nanocomposites of SnO$_2$ and g-C$_3$N$_4$: Preparation, characterization and photocatalysis under visible LED irradiation. *Ceram. Int.* **2018**, *44*, 3837–3846. [CrossRef]
19. Qi, K.; Liu, S.-y.; Zada, A. Graphitic carbon nitride, a polymer photocatalyst. *J. Taiwan Inst. Chem. Eng.* **2020**, *109*, 111–123. [CrossRef]
20. Wang, G.; Long, X.; Qi, K.; Dang, S.; Zhong, M.; Xiao, S.; Zhou, T. Two-dimensional CdS/g-C$_6$N$_6$ heterostructure used for visible light photocatalysis. *Appl. Surf. Sci.* **2019**, *471*, 162–167. [CrossRef]
21. Zhao, K.; Khan, I.; Qi, K.; Liu, Y.; Khataee, A. Ionic liquid assisted preparation of phosphorus-doped g-C$_3$N$_4$ photocatalyst for decomposition of emerging water pollutants. *Mater. Chem. Phys.* **2020**, *253*, 123322. [CrossRef]
22. Chang, S.; Sang, Y.; Liu, H. Efficient Photocatalytic Degradation of RhB by Constructing Sn$_3$O$_4$ Nanoflakes on Sulfur-Doped NaTaO$_3$ Nanocubes. *Crystals* **2021**, *11*, 59. [CrossRef]
23. Wierzbicka, E.; Syrek, K.; Mączka, K.; Sulka, G.D. Photocatalytic Decolorization of Methyl Red on Nanoporous Anodic ZrO$_2$ of Different Crystal Structures. *Crystals* **2021**, *11*, 215. [CrossRef]

24. Alharthi, F.A.; Alanazi, H.S.; Alsyahi, A.A.; Ahmad, N. Hydrothermal Synthesis, Characterization and Exploration of Photocatalytic Activities of Polyoxometalate: Ni-CoWO$_4$ Nanoparticles. *Crystals* **2021**, *11*, 456. [CrossRef]

25. Yang, Y.; Li, Y.; Zhu, L.; He, H.; Hu, L.; Huang, J.; Hu, F.; He, B.; Ye, Z. Shape control of colloidal Mn doped ZnO nanocrystals and their visible light photocatalytic properties. *Nanoscale* **2013**, *5*, 10461–10471. [CrossRef] [PubMed]

26. Miao, L.; Shi, B.; Stanislaw, N.; Mu, C.; Qi, K. Facile synthesis of hierarchical ZnO microstructures with enhanced photocatalytic activity. *Mater. Sci.-Pol.* **2017**, *35*, 45–49. [CrossRef]

27. Qi, K.; Cheng, B.; Yu, J.; Ho, W. Review on the improvement of the photocatalytic and antibacterial activities of ZnO. *J. Alloys Compd.* **2017**, *727*, 792–820. [CrossRef]

28. Liu, X.; Xu, H.; Li, D.; Zou, Z.; Xia, D. Facile Preparation of BiOCl/ZnO Heterostructure with Oxygen-Rich Vacancies and Its Enhanced Photocatalytic Performance. *Chem. Sel.* **2019**, *4*, 12245–12251. [CrossRef]

29. Qi, K.; Liu, S.-y.; Selvaraj, R.; Wang, W.; Yan, Z. Comparison of Pt and Ag as co-catalyst on g-C3N4 for improving photocatalytic activity: Experimental and DFT studies. *Desalin. Water Treat.* **2019**, *153*, 244–252. [CrossRef]

30. An, C.; Peng, S.; Sun, Y. Facile Synthesis of Sunlight-Driven AgCl:Ag Plasmonic Nanophotocatalyst. *Adv. Mater.* **2010**, *22*, 2570–2574. [CrossRef]

31. Zhang, S.; Khan, I.; Qin, X.; Qi, K.; Liu, Y.; Bai, S. Construction of 1D Ag-AgBr/AlOOH Plasmonic Photocatalyst for Degradation of Tetracycline Hydrochloride. *Front. Chem.* **2020**, *8*, 117. [CrossRef]

32. Boltersdorf, J.; Leff, A.C.; Forcherio, G.T.; Baker, D.R. Plasmonic Au–Pd Bimetallic Nanocatalysts for Hot-Carrier-Enhanced Photocatalytic and Electrochemical Ethanol Oxidation. *Crystals* **2021**, *11*, 226. [CrossRef]

33. Zada, A.; Muhammad, P.; Ahmad, W.; Hussain, Z.; Ali, S.; Khan, M.; Khan, Q.; Maqbool, M. Surface Plasmonic-Assisted Photocatalysis and Optoelectronic Devices with Noble Metal Nanocrystals: Design, Synthesis, and Applications. *Adv. Funct. Mater.* **2019**, *30*, 1906744. [CrossRef]

34. Christopher, P.; Ingram, D.B.; Linic, S. Enhancing Photochemical Activity of Semiconductor Nanoparticles with Optically Active Ag Nanostructures: Photochemistry Mediated by Ag Surface Plasmons. *J. Phys. Chem. C* **2010**, *114*, 9173–9177. [CrossRef]

35. Ren, C.; Yang, B.; Wu, M.; Xu, J.; Fu, Z.; Lv, Y.; Guo, T.; Zhao, Y.; Zhu, C. Synthesis of Ag/ZnO nanorods array with enhanced photocatalytic performance. *J. Hazard. Mater.* **2010**, *182*, 123–129. [CrossRef]

36. Rupa, A.V.; Manikandan, D.; Divakar, D.; Sivakumar, T. Effect of deposition of Ag on TiO$_2$ nanoparticles on the photodegradation of Reactive Yellow-17. *J. Hazard. Mater.* **2007**, *147*, 906–913. [CrossRef] [PubMed]

37. Qi, K.; Xing, X.; Zada, A.; Li, M.; Wang, Q.; Liu, S.-Y.; Lin, H.; Wang, G. Transition metal doped ZnO nanoparticles with enhanced photocatalytic and antibacterial performances: Experimental and DFT studies. *Ceram. Int.* **2020**, *46*, 1494–1502. [CrossRef]

38. He, G.; Xing, C.; Xiao, X.; Hu, R.; Zuo, X.; Nan, J. Facile synthesis of flower-like Bi$_{12}$O$_{17}$Cl$_2$/β-Bi$_2$O$_3$ composites with enhanced visible light photocatalytic performance for the degradation of 4-tert-butylphenol. *Appl. Catal. B Environ.* **2015**, *170*, 1–9. [CrossRef]

39. Kong, L.; Yu, B.; Xu, X.; Pan, J.; Su, Y.; Hu, J. Room Temperature Ferromagnetism and Photoluminescence in Cu-Doped ZnO Nanocrystals. *J. Nanosci. Nanotechnol.* **2014**, *14*, 6012–6015. [CrossRef] [PubMed]

40. Jiang, D.; Wang, T.; Xu, Q.; Li, D.; Meng, S.; Chen, M. Perovskite oxide ultrathin nanosheets/g-C$_3$N$_4$ 2D-2D heterojunction photocatalysts with significantly enhanced photocatalytic activity towards the photodegradation of tetracycline. *Appl. Catal. B Environ.* **2017**, *201*, 617–628. [CrossRef]